PAPER • OPEN ACCESS

Image pre-processing method for near-wall PIV measurements over moving curved interfaces

To cite this article: L C Jia *et al* 2017 *Meas. Sci. Technol.* **28** 035201

View the article online for updates and enhancements.

Image pre-processing method for near-wall PIV measurements over moving curved interfaces

L C Jia, Y D Zhu, Y X Jia, H J Yuan and C B Lee

State Key Laboratory for Turbulence and Complex Systems, College of Engineering, Peking University, Beijing Shi, People's Republic of China and Advanced Aero Engine Collaborative Innovation Center

E-mail: cblee@mech.pku.edu.cn

CrossMark

Abstract

PIV measurements near a moving interface are always difficult. This paper presents a PIV image pre-processing method that returns high spatial resolution velocity profiles near the interface. Instead of re-shaping or re-orientating the interrogation windows, interface tracking and an image transformation are used to stretch the particle image strips near a curved interface into rectangles. Then the adaptive structured interrogation windows can be arranged at specified distances from the interface. Synthetic particles are also added into the solid region to minimize interfacial effects and to restrict particles on both sides of the interface. Since a high spatial resolution is only required in high velocity gradient region, adaptive meshing and stretching of the image strips in the normal direction is used to improve the cross-correlation signal-to-noise ratio (SN) by reducing the velocity difference and the particle image distortion within the interrogation window. A two dimensional Gaussian fit is used to compensate for the effects of stretching particle images. The working hypothesis is that fluid motion near the interface is 'quasi-tangential flow', which is reasonable in most fluid-structure interaction scenarios. The method was validated against the window deformation iterative multi-grid scheme (WIDIM) using synthetic image pairs with different velocity profiles. The method was tested for boundary layer measurements of a supersonic turbulent boundary layer on a flat plate, near a rotating blade and near a flexible flapping flag. This image pre-processing method provides higher spatial resolution than conventional WIDIM and good robustness for measuring velocity profiles near moving interfaces.

Keywords: moving curved interfaces, near-wall PIV measurements, image transformation, adaptive stretching, synthetic particles

(Some figures may appear in colour only in the online journal)

1. Introduction

The important roles of boundary effects in instability development, vorticity generation, and in heat and mass transfer have attracted the interest of many researchers [10]. Accurate flow measurements at or very near rigid surfaces are essential for understanding fluid-structure interactions, such as fish swimming, flag flapping, falling disks [22, 29], or turbomachinery [11, 26–28]. In the past two decades, PIV has become a powerful tool for measuring fluid velocities owing to its non-intrusive nature [1]. However, PIV measurements near a wall are still a great challenge due to strong wall reflections of laser light and high-shear gradients. The situation becomes more difficult when the interface is moving and curved, which is typical of turbomachinery. The inherent geometric complexity of turbine blade makes strong wall reflections inevitable. Also,

dramatic changes in direction and magnitude of the velocity lead to high shear stresses along the blade surfaces.

Since setup modifications are not always possible or become impractical when dealing with curved interfaces, methods have been proposed to minimize the influence of undesired light reflection. The elimination of interfaces with a digital mask technique [5, 6] and the relocation method [7] have been utilized to improve the measurement accuracy in the near-wall region. However, the position of moving interface must first be accurately determined before further processing of the image strips near the interface. Jeon and Sung [9] transformed the particle images into Cartesian coordinates that were related to the distance from interface. Park *et al* [16] extended this method to PIV measurements of the flow around free surfaces. As demonstrated by [30–32] and [23], the optimal synthetic particles (OSP) method can improve predictions of the velocity distributions for high-shear flows near a stationary interface. This technique is also used for the interface treatment in this study.

A variety of attempts have been made to increase the cross-correlation signal in high-shear regions where tracer patterns deform. Huang *et al* [8] presented a particle image distortion (PID) technique to distort a particle image according to the initially calculated velocity field to compensate for the estimated deformation. Scarano and Riethmuller [21] balanced the conflict between dynamic range and spatial resolution with a multigrid cross-correlation scheme with a discrete window offset. Then, [19] combined the PID technique with a multigrid scheme to develop the window deformation iterative multi-grid scheme (WIDIM), which significantly improved signal-to-noise ratio of the cross-correlation results. Nguyen and Wells [14, 15] proposed the IPX/IG method to directly measure the shear rate by shearing the PIV image templates parallel to non-slip and curved walls. Then, [12, 15] proposed interfacial PIV (IPIV) to extract both the wall-shear gradient and the near-wall tangential and wall normal velocity profiles at one pixel resolution.

Few attempts have been reported in the literature to adapt the cross-correlation analysis by modifying the window size and orientation. Rohály *et al* [17] adapted the window size to the correlation signal within a hierarchical structure. An algorithm to vary the interrogation window size with respect to local velocity fluctuations was proposed by [19]. The window shape was adapted to the flow direction [3] or the velocity field curvature [20]. Theunissen *et al* [24, 25] proposed an adaptive interrogation methodology based on the local signal content and local flow conditions to maximize the wall-normal spatial resolution which can be used for inclined and curved interfaces. However, adaptive domain discretization with unstructured meshing is not easy to implement and time-consuming, compared with the application of hierarchical schemes for multi-resolution analysis of PIV images.

The image pre-processing method developed in the present study is an extension of the **OSP** method with a conformal transformation of particle images and adaptive image meshing and stretching in the normal direction along a curved interface. The influence of the transformation and adaptive stretching of particle images on the cross-correlation peak is also discussed. A two dimensional Gaussian fit algorithm is used to obtain a
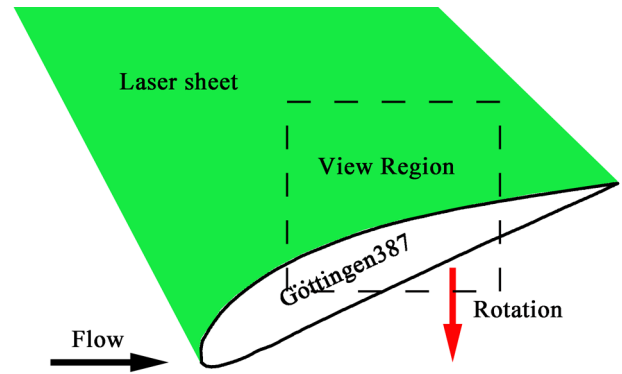

Figure 1. Schematic of a rotating blade flow.

reliable displacement estimate of the stretched particle images. Synthesized images of laminar flow over a curved interface shown in figure 1 are used to investigate the capabilities of this method for measuring near-wall profiles. Finally, the method is further tested by three real flows of a hypersonic turbulent boundary layer on a flat plate, laminar flow around a curved blade and turbulent flow over a flapping flag.

2. Method description

The image pre-processing method consists of 6 steps:

(1) identify the interface position
(2) transform the particle image strips near the interface to Cartesian coordinates
(3) calculate transformed images using WIDIM to obtain the initial velocity distribution
(4) generate adaptive stretched images based on the velocity distribution obtained in step 3
(5) calculate adaptive stretched images to get the velocity profiles in the near-wall region
(6) reverse transform the velocity profile obtained in the transformed domain to physical domain

Steps 3–5 are iterated until the result converges to a steady value. Various image transformation methods have been proposed, such as trapezoidal transformation [9] and conformal transformation [12], which correspond to step 3 in this method. As shown later, transforming the near-wall image region to a rectangular shape improves the predicted PIV velocity profiles within the boundary layer. However, the adapted stretching of particle image strips used here gives even better predictions of velocity distribution for high-shear flows near the interface. Detailed descriptions of these steps are presented in the following sections.

2.1. Interface tracking

The interface identification accuracy strongly affects the effectiveness of the **OSP** method and velocity prediction accuracy in near-wall PIV measurements. For a simple fixed interface, the location can be detected manually, such as the case for a flat plate. However, an automatic identification method is necessary when the interface is moving arbitrarily.
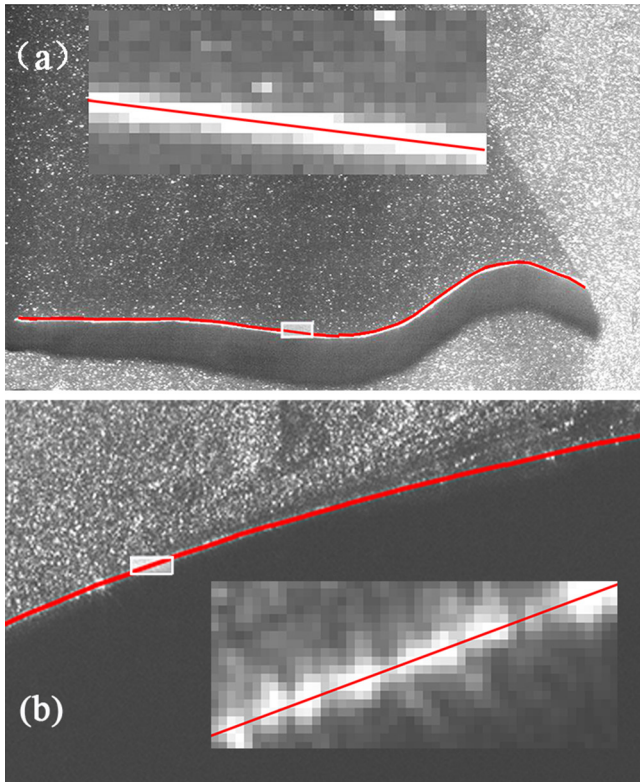
Figure 2. Interfaces detected by the Random transform, with a closeup of the white rectangular zone. (a) Curved interface of a flapping flag, (b) curved interface of a rotating blade.

In an image set, the interface position can be extracted by using an iterate Radon transformation (Arnaud and Atle 2011). This method is easier to implement than contour-texture analysis [9] when there are significant intensity differences between the wall region and fluid region, such as the interface of a flat plate, a rotating blade or a flapping flag. Intensity fluctuations due to the particles tend to be canceled out by the integration process. Typically, the curved interface can be represented by several straight line segments. Since radon transform integrates the intensity along a straight line, the interface curvature must not be too large for precise interface tracking. At the same time, the segments should not be too long. Experience has shown that a segment length of 16 pixels works best in our experiments. Here, discrete position points are curve-fitted to obtain a continuous interface for the trapezoidal transformation. Two different functions were used, a third order polynomial function for the blade and a spline function for the flapping flag. Figure 2 shows the detected boundary from experimental images for the rotating blade surface and the flapping flag surface.

2.2. Transformation of the near wall region to Cartesian coordinates

Analyses of PIV images for a moving body require regularized coordinates for uniform application of the very effective hierarchical schemes for multi-resolution analyses of PIV images. The wall-normal (n) and wall-parallel (s) directions are chosen as the axes of the regularized coordinate system. The image transformation converts the near-wall curved
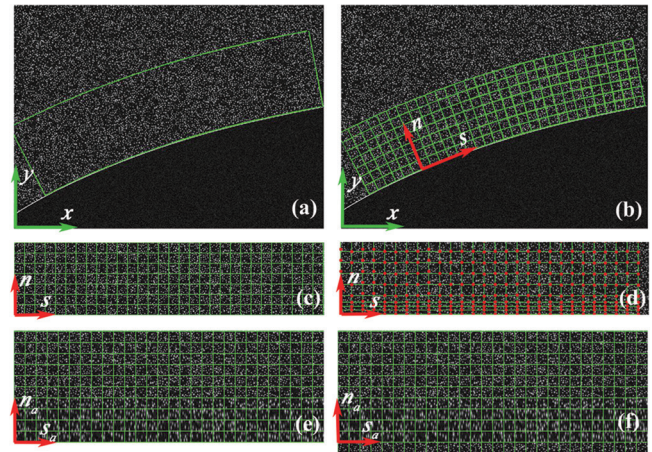

Figure 3. Image transformation and adaptive stretching method to deal with curved interfaces. (a) curved interface in the near-wall region in (x, y) space for a rotating blade, (b) trapezoidal mesh generated from the interface points, (c) transformed image in the regularized coordinates, (d) adaptive grid generated in the normal direction, (e) adaptive stretching image in the regularized coordinates, (f) adaptively stretched image with synthetic particles added in the solid body.

image strips in physical domain (x, y) to regularized coordinates in transformed domain (s, n).

The image transform algorithm proposed by [9] was used to transform the curvilinear interface in PIV image into a straight interface in Cartesian coordinates. For simplicity, the bottom side of the grid mesh was chosen to be on the curved interface with the top side chosen to enclose a region with a fixed height. The sidewalls are coincident with the local normal lines of the interface as illustrated in figure 3(a). After the segment lengths were determined, the mesh in figure 3(b) was generated. Then, pixel intensities at the grid points were interpolated to produce the rectangular image shown in figure 3(c).

2.3. Calculating transformed images

The transformed particle images from step 2 were analyzed using the WIDIM [19] algorithm. This technique allows progressive refinement of the window size. As a result, the method progressively compensates for the in-plane flow motion with smaller interrogation windows at each iteration. The image processing was performed with three image distortion iterations. For standard situations, the interrogation window size ($w_s \times w_n$) ranges from 64×64 pixels to 32×32 pixels with an overlap factor of 75% applied between adjacent windows. The errors in the displacements are acceptable except at the border points. Although the interface velocity can be determined from the physical displacement (Δx, Δy) of the interface, some sub-pixel errors in the displacements still remain. Thus, the PIV/IG [13, 14] method was used in the present study to evaluate the interface displacements.

2.4. Generating adaptively stretched images

This section describes a flow-adaptive spatial resolution method along the wall-normal direction. For quasi-tangential flow, as in the situations discussed here, local velocity gradients
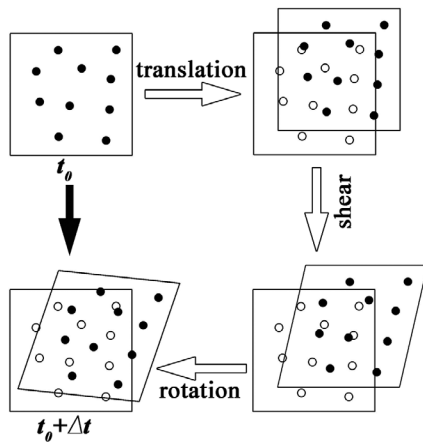
Figure 4. Schematic illustration of the motion of particles within an interrogation window.

Figure 5. Schematic of the effects of the transformation and adaption on the correlation peak detection.

along the wall-normal direction are taken into account to locally increase the interrogation spatial density. Instead of reducing the local interrogation window size, adaptive stretching of the image strips is used based on the local velocity gradient. A threshold gradient of the wall-parallel velocity component is used to determine the adaptive mesh grid positions along wall-normal directions. Then, the interrogation window size $w_n(s, n)$ varies along n direction at each s position, with $w_s(s, 0)$ kept constant. The velocity distribution along n direction at different s positions results in some fluctuations of the the window size distribution in normal direction as the red dots in figure 3(d). The spatially averaged distribution of $\overline{w_n(s, n)}$ is used for the entire particle image. Then, all the different size image templates ($w_s \times w_n$) are stretched into cubic image templates ($w_s \times w_s$) as shown in figure 3(e). The relation between the transformed image and the adaptively stretched image is represented by a matrix A defined as:

$$(s, n) = A(s_a, n_a) \tag{1}$$

in which

$$A = \begin{pmatrix} 1 & 0 \\ 0 & w_n/w_s \end{pmatrix} \tag{2}$$

Synthetic particles with kinetic information of the solid body are generated under the interface, as shown in figure 3(f), to provide an effective velocity reference in the near-wall region.

The adaptive mesh grid distribution is based on the criterion:

$$w_n = \min(w_n^*, w_s) \tag{3}$$

where

$$w_s = \left(n_{\text{top}} - n_{\text{bottom}}; \left| \frac{U(n_{\text{top}}) - U(n_{\text{bottom}})}{U_{\text{gradient}}} \right| \leqslant \varepsilon \right) \tag{4}$$

and $w_n^* = 9$ pxiels is the minimum distance needed to keep a sufficient number of particles in an interrogation window. Taking $U_{\text{gradient}} = 0.2 U_{\text{mainstream}}$ as an example, the window aspect ratio is in the range of 1 to 4 along the normal direction, which is consistent with results of the adaptive sampling and windowing interrogation method proposed by [25].
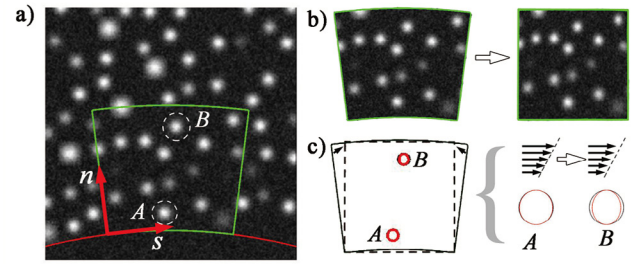
2.5. Calculating adaptively stretched images

2.5.1. Effects of the transformation and adaptive stretching on particle images.
Considering flow characteristics of the near wall flow around a curved interface, particle motion within an interrogation window can be devided into three parts: mean displacement (translation), local displacement gradient (shear) and rotation, as shown in figure 4. The widely used multigrid image deformation method typically work best when the first two factors are taken into consideration. However, for flows along a curved interface, where rotation between neighbouring interrogation windows is inevitable, rotation effect can be reduced by transforming the curved investigation domain into a rectangular domain.

For the originally fan-shaped particle image illustrated in figure 5(a), the transformation algorithm generates a new Cartesian coordinate system image that regularizes the fan-shaped image into a wall-parallel direction, s, and a wall-normal direction, n, as shown in figure 5(b). However, the transformation distorts the velocity distribution and intensity distribution of the particles within the interrogation window. Take the convex surface shown in figure 5(c) for example, stretching ratio is different at the upper and lower parts of the fan-shape image, so the particle image strips and the velocities both shrink more in the upper part. Two points at different normal positions are used to show the particle shape distortion. Significant difference can be found between these two target objects. The particle distortion also exists for a concave surface and the velocity difference within an interrogation window will further increase as the curvature decrease. Both of these distortions will lead to inaccurate cross-correlation peak detection. A dimensionless parameter, D_r, was defined based on the linear assumption to characterize the distortion as:

$$D_r = \frac{R_{\text{upper}}}{R_{\text{lower}}} = \frac{R_{\text{lower}} + w_n}{R_{\text{lower}}} \tag{5}$$

where, R_{lower} is radius of curvature of the lower interface, R_{upper} is radius of curvature of the upper interface and w_n is interrogation window size in the normal direction. When large enough, the curvature has little influence on the transformation since D_r approaches unity, as has been verified in particle images near a straight interface or far from curved bodies. Unfortunately, a larger D_r is inevitable near a curved surface. Thus, an acceptable level of image distortion should
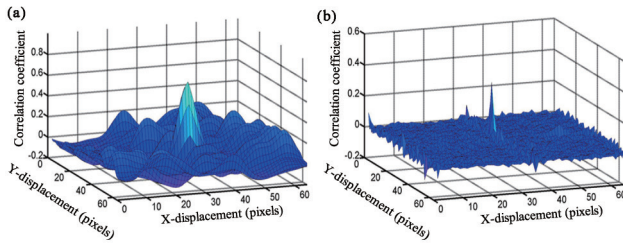
Figure 6. Correlation maps corresponding to different correlation peak detection algorithms: (a) normal cross correlation method, (b) correlation peak detection with phase fit.

be specified when the adaptive stretching algorithm reduces the window size in normal direction near interface.

Thus, the adaptive stretching technique has several advantages with respect to a basic correlation method: (a) velocity gradient within an interrogation window is reduced; (b) rotation effect of the particle image patterns is weakened; and (c) distortion ratio of a single interrogation window converges to unity even near a curved interface.

2.5.2. Correlation peak detection of adaptively stretched particle images. A more robust method to get sub-pixel accuracy when estimating the position of correlation peak is to fit the correlation data to some function. For an undistorted particle image, the most frequently implemented three-point estimator is the Gaussian peak fit. However, for elliptically shaped peaks, the two one-dimensional fits will not return the correct peak center. An alternative peak location estimator, which provides higher accuracy than these previous methods is to fit a two-dimensional Gaussian, as introduced by [18]. A direct result of the adaptive stretching of images is the wide Gaussian bells in the correlation distribution, as shown in figure 6(a). If the assumption that all particle images inside the interrogation area have the same shape, the position and height of the correlation peak can be computed with a phase fit algorithm [4], as shown in figure 6(b). For the adaptive stretching of particle images near a straight interface, the assumption that all particle images inside the interrogation area have the same shape can be satisfied if the particle displacement gradients are not too large. However, the nonuniform distortion of particle images caused by the transformation algorithm will lead to some deviations from the assumption. So, an adaptive stretching method is needed for PIV measurements near a curved interface.

2.5.3. WIDIM algorithm. The conventional WIDIM technique with these steps can be used directly on the adaptively stretched images. Both the particle image distortion technique and interrogation overlap technique are used in this step to effectively improve the measurement spatial resolution in normal direction. The reduced velocity gradient within a single interrogation window gives better cross-correlation peak detection based on the adaptively stretched images. PIV results in (*s,n*) domain for step 3 and step 5 at the same *s* position are compared in figure 7.

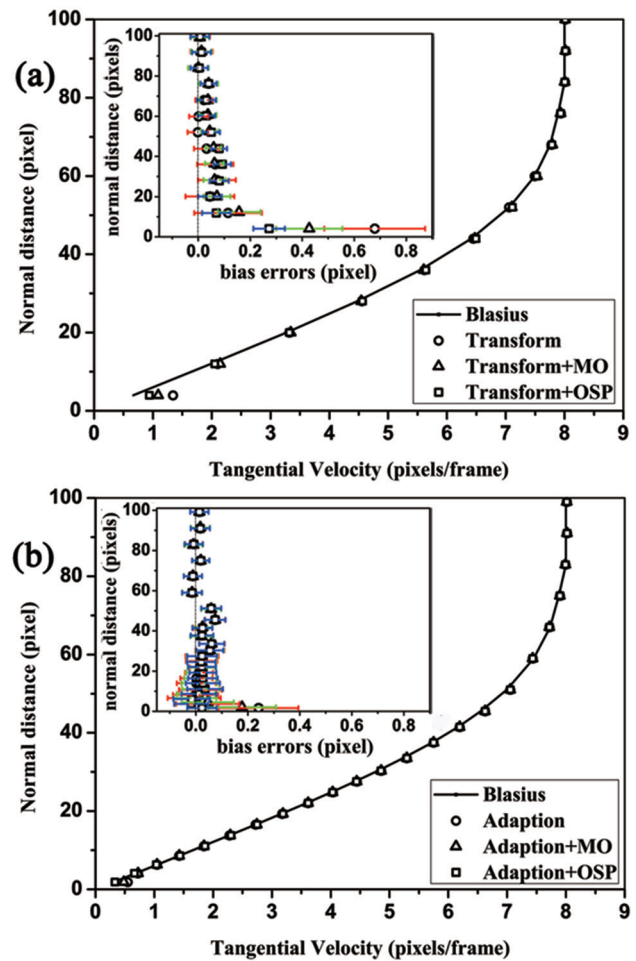Three pre-processing methods were used with the original images (Transform, Adaption), the digital mask technique

Figure 7. Estimated displacement profiles and bias error distributions for an imposed Blasius boundary layer based on: (a) transformed images (step 3), (b) adaptively stretched images (step 5).

(Transform + **MO**, Adaption + **MO**) and the **OSP** method (Transform + **OSP**, Adaption + **OSP**). For both the transformed images and the adaptively stretched images, synthetic particles in the solid body provide the best agreement with the imposed velocity distribution, especially in the near-wall region. The root-mean-square (RMS) distributions from **OSP** method are also smaller than **MO** method. As mentioned earlier, the adaptive stretching method provides more interrogation points inside the shear layer, so more velocity vectors can be acquired as shown in figure 7(b). The reduction of velocity difference in a single interrogation window leads to most of the bias errors in figure 7(b) being less than 0.05 pixel. Thus, two main benefits of the adaptive stretching pre-processing method are a higher spatial resolution and lower bias errors in the near-wall region.

2.6. Reverse transform to the physical domain

The relation between physical displacement (*u*, *v*) and the corresponding displacement (*U*, *V*) in the final adaptively stretched domain can be expressed by an alternative method which represents the transformation of a particular position

$(x(s, n), y(s, n))$ by the stretching factors in two orthogonal directions (S_x, S_y) and the rotation angle (α). The stretching factors from the physical interrogation window length are defined as:

$$S_x = \sqrt{\frac{1}{2}\{[\frac{\Delta x(s, n)}{\Delta w_s(s, n)}]^2 + [\frac{\Delta x(s, n+1)}{\Delta w_s(s, n+1)}]^2\}}$$

$$S_y = \sqrt{\frac{1}{2}\{[\frac{\Delta y(s, n)}{\Delta w_n(s, n)}]^2 + [\frac{\Delta y(s+1, n)}{\Delta w_n(s+1, n)}]^2\}} \quad (6)$$

Rotation angle of the interrogation widow is obtained from inclinations of the four sides of the interrogation window as:

$$\alpha = \frac{1}{2}\{\text{atan}[\frac{\Delta y(s, n)}{\Delta x(s, n)}] + \text{atan}[\frac{\Delta y(s, n+1)}{\Delta x(s, n+1)}]\} \quad (7)$$

3. Validation with synthetic images

This image pre-processing method was designed to deal with velocity measurements in flows near moving curved walls. The rest of the paper focuses on validations of this method for resolving velocity profiles using the WIDIM technique near interfaces with different sets of transformed images.

3.1. Creation of the synthetic particle images

A synthetic image set was used to assess the effects of different pre-processing methods. The flow region had a particle density of 0.02 particles per pixel^2. The particles were distributed randomly in a light sheet centered at $z = 0$. The light sheet had a Gaussian intensity distribution with a maximum intensity of 256, corresponding to an 8 *bit* sensor. Background noise was added with an average of 16% and fluctuations of 5% of the maximum intensity. One hundred synthetic image pairs with 1024 pixels × 1024 pixels were generated covering a field of view of $H \times H$, where H was 20 mm. The synthetic images were generated along a curved surface (Göttingen387 profile). The displacement profile of the boundary layer obeys the Blasius solution with a thickness of 80 pixels, as in real experiments. The mainstream velocities, (U_m), used here were 8, 16 and 24 pixels/frame. The first simulated exposure captured the projection of the initial tracer positions. The second exposure again captured the projected tracers displaced according to the spatial interpolation of the 2D velocity field. The intensity distribution for each particle was interpolated from the Gaussian function. An example of the generated images is shown in figure 3(a). The synthetic particle image generation technique was also applied to synthetic particles in the solid body. Tests gave $0.2u$ as the critical threshold gradient to generate adaptively stretched particle images. The window size in s direction w_s was 32 pixels.

3.2. Evaluation algorithm

Four particle image sets were used to evaluate the velocity profiles near the interfaces and illustrate the importance of the additional particles in the solid region, the original synthetic
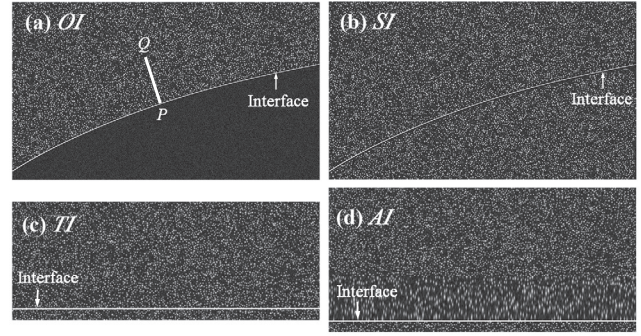

Figure 8. Different interface preprocessing methods: (a) original synthetic particle images (**OI**), (b) particle images with added synthetic particles in the solid body (**SI**), (c) transformed images with added synthetic particles (**TI**) and (d) adaptive stretched images with added synthetic particles (**AMSI**).

particle images (OI), particle images with synthetic particles added in the solid body (SI), transformed images with synthetic particles added in the solid body (TI) and adaptive stretched images with added synthetic particles (AMSI), as shown in figure 8. The WIDIM scheme used a one pass interrogation with a 64 × 64 pixels window and two passes with a 32 × 32 pixels window with 75% overlap between horizontally and vertically adjacent windows.

The velocity measurement errors were quantified by a random error distribution, $\epsilon(s)_{u,\text{rand}}$, defined as the rms of the difference between $u(s, n)_p$ and their ensemble average expressed as:

$$\epsilon(s)_{u,\text{rand}} = \sqrt{\frac{1}{NP}\sum_{n=1}^{N}\sum_{p=1}^{P}(u(s, n)_p - \overline{u(s, n)_p})^2} \quad (8)$$

in which $P = 100$ is the number of velocities obtained from 100 synthetic image pairs, N is the number of velocity points in the wall-normal direction, and the ensemble-averaged velocity, $\overline{u(s, n)_p}$, is defined as:

$$\overline{u(s, n)_p} = \frac{1}{P}\sum_{p=1}^{P}u(s, n)_p \quad (9)$$

The total error, $\epsilon(s)_{u,\text{total}}$, was defined as the rms of the difference between $u(s, n)_p$ and the true velocity $U(s, n)_p$ expressed as:

$$\epsilon(s)_{u,\text{total}} = \sqrt{\frac{1}{NP}\sum_{n=1}^{N}\sum_{p=1}^{P}(u(s, n)_p - U(s, n)_p)^2} \quad (10)$$

Similar random and total errors for v were obtained as in equations (8) and (10) by replacing $u(s, n)_p$ by $v(s, n)_p$, $\overline{u(s, n)_p}$ by $\overline{v(s, n)_p}$ and $U(s, n)_p$ by $V(s, n)_p$.

3.3. Results and discussion

For flow-structure interaction problems, the relative velocity distribution plays an important role in understanding the physical mechanism. The work of [9] was used to find the interface velocity, which was used to add the synthetic particles as
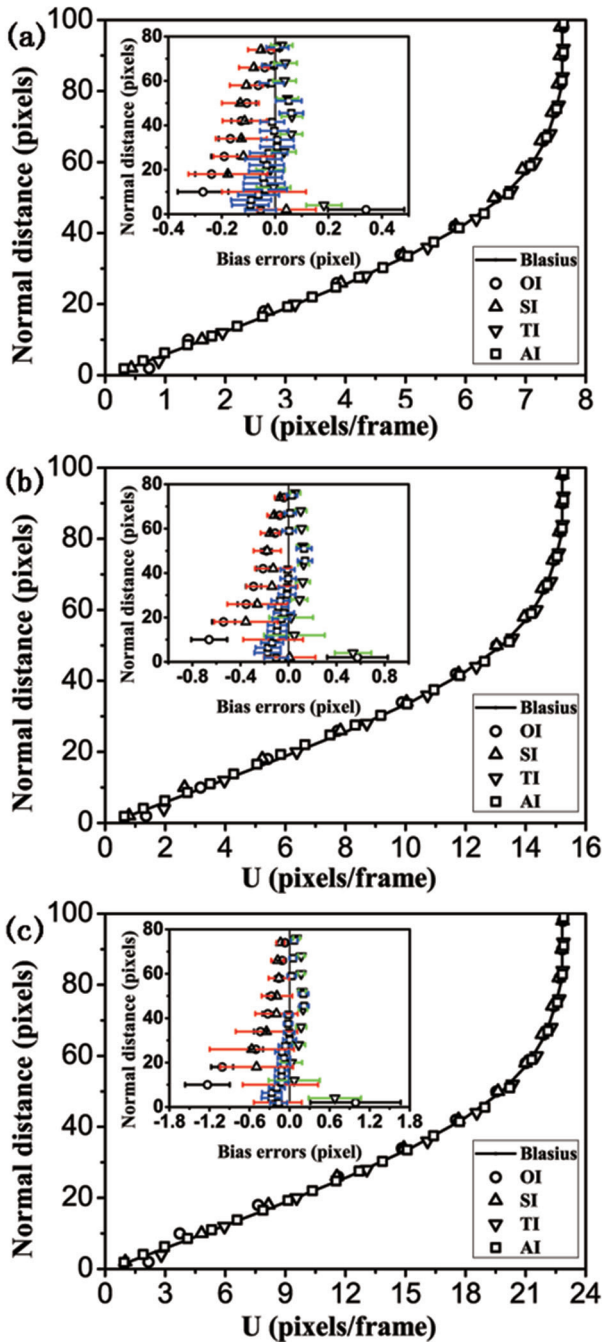
Figure 9. *x*-direction relative velocity profiles and bias error distributions in the physical domain (*x, y*) based on the different image processing methods. (a) $U_m = 8$ pixels/frame, (b) $U_m = 16$ pixels/frame, (c) $U_m = 24$ pixels/frame.

mentioned earlier. The rest of this paper focuses on improving prediction of the relative velocity distribution in near-wall region.

Figure 9 shows PIV measurement results along the wall-normal line *PQ* shown in figure 8(a) by different particle images: OI (circles), SI (triangles), TI (inverted triangles), AMSI (squares) and the true values (circular). *u* component profiles in the physical domain (*x,y*) are given for different U_m. The bias errors represent the deviations of the measured values from the imposed values. The error bars show the random error distribution, $\epsilon(s)_{u,\text{rand}}$, for different measurements.

Table 1. rms errors for different image pre-processing methods along a curved interface.

U_m	rms	OI	SI	TI	AMSI
8	$\epsilon_{u,\text{total}}$	0.250 38	0.217 94	0.082 63	0.065 07
16	$\epsilon_{u,\text{total}}$	0.488 22	0.405 80	0.303 26	0.115 63
24	$\epsilon_{u,\text{total}}$	0.871 55	0.642 24	0.412 11	0.214 24
8	$\epsilon_{v,\text{total}}$	0.084 02	0.073 52	0.037 44	0.046 28
16	$\epsilon_{v,\text{total}}$	0.142 77	0.136 56	0.106 91	0.061 98
24	$\epsilon_{v,\text{total}}$	0.259 00	0.208 57	0.153 16	0.107 90

Table 2. rms errors for different image pre-processing methods along a straight interface.

U_m	rms	SI	AMSI
8	$\epsilon_{u,\text{total}}$	0.093 18	0.069 02
16	$\epsilon_{u,\text{total}}$	0.215 36	0.124 72
24	$\epsilon_{u,\text{total}}$	0.405 52	0.203 66
8	$\epsilon_{v,\text{total}}$	0.032 79	0.038 28
16	$\epsilon_{v,\text{total}}$	0.041 83	0.040 77
24	$\epsilon_{v,\text{total}}$	0.067 03	0.051 46

Velocity measurements from all four image types generally agree well with the imposed velocity distribution beyond the boundary layer region. However, significant differences in the velocity predictions by different pre-processing methods are seen in the near-wall region. The improvement by adding synthetic particles is seen by comparing the OI and SI results. The improvement is more obvious closer to the interface. Both the TI and AMSI methods reduce the bias errors by almost 50%, compared with the OI method. The AMSI measurements provide higher spatial resolution and smaller bias errors than TI, with only a small increase in $\epsilon(s)_{u,\text{rand}}$ due to reduction in the number of particles within the interrogation window. This tendency is also observed for higher U_m, as shown in figures 9(b) and (c). The bias errors and random errors increase as the mainstream velocity increases. This can be explained by more serious image deformation within a single interrogation window for higher shear rates. The same phenomenon is also seen for the *v* component distributions in the physical domain.

The effectiveness of the AMSI method is illustrated by comparing the total errors ($\epsilon_{u,\text{total}}$ and $\epsilon_{u,\text{total}}$) of these four methods along line *PQ* as shown in table 1. The total errors for both the TI and AMSI methods are much less than those of OI and SI. For higher mainstream velocities, the total errors decrease from left to right for a given U_m. As the mainstream velocity increases, the total errors of these four pre-processing methods grow in different ways. The PIV results within the boundary layer based on the AMSI images are considerably more accurate than for the other image pre-processing methods for both *u* and *v* components. Even for the highest mainstream velocity, 24 pixels/frame, the total errors of the AMSI method are still at an acceptable level, with $\epsilon_{u,\text{total}}$ of 0.214 pixels and $\epsilon_{v,\text{total}}$ of 0.108 pixels.

The rms errors for a curved interface can be compared with those for a straight interface, using the same flow as in the curved interface, in tables 1 and 2. Considering the improved velocity distribution prediction by **OSP** method,
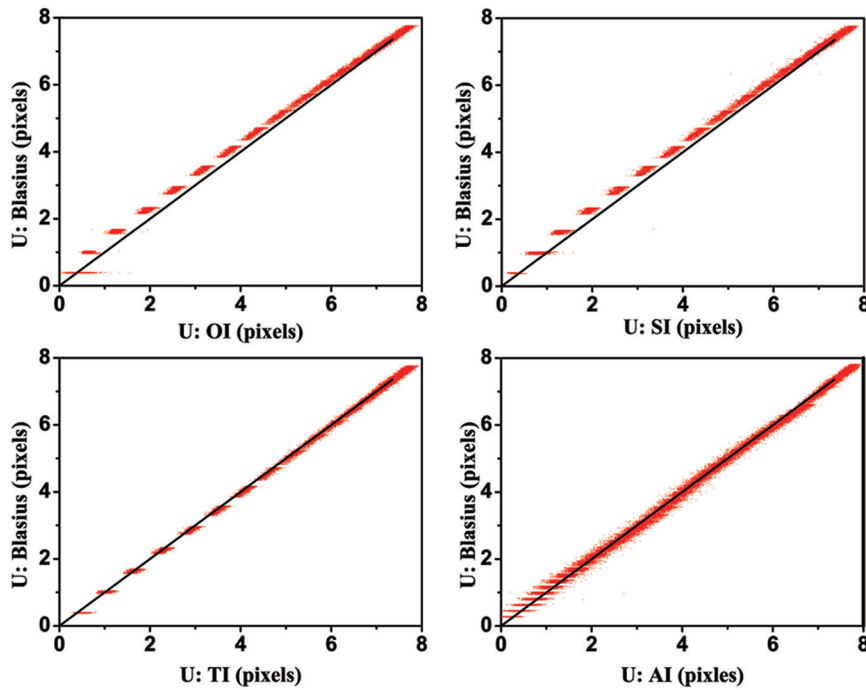
Figure 10. Point-to-point comparisons of displacements in the physical domain against those given by the Blasius velocity profile from 100 synthetic image pairs along the blade surface within 80 pixels ($U_m = 8$ pixels/frame). (a) OI, (b) TI, (c) SI, (d) AMSI.

the OI results are not discussed here. Both tables used the same cross-correlation algorithm and the same interrogation window setup. More obvious improvements are seen in the total random errors results for SI and AMSI methods for the curved interface compared with the straight interface. This can be explained by the benefits of reduced velocity gradient, particle image distortion and correlation of the rotation of the original image strips.

The cause of differences in the total errors is shown by a more detailed comparison between the *u* velocity component measurements based on the different particle images in figure 10 for measurement points less than 80 pixels from the interface. The results are similar for different mainstream velocities, so only the $u_m = 8$ pixels/frame case is shown here. The measurements using OI (figures 8(a)) and SI (b) significantly differ from the true velocity, especially for high-shear cases, with total errors $\epsilon_{u,\text{total}} = 0.872$ and 0.642 pixels. The bias errors between measurement and imposed values are responsible for the higher total errors. The improvement with SI images comes from the synthetic particle restriction in near-wall region. The total error is reduced to 0.412 pixels for the TI images, as shown in figure 10(c). This is due to more accurate prediction of the true velocity. Finally, the total error is reduced to 0.214 pixels for the AMSI images as shown in figure 10(d), equivalent to 1/4 of the total error of OI case, 1/3 of the total error of SI case and 1/2 of the total error of TI case. This improvement is mainly due to reduced velocity gradient in the adaptively stretched images. The same tendency is seen in *v* component velocity profiles.

The distributions of bias errors ($\beta(u)$ and $\beta(v)$) and random errors ($\sigma(u)$ and $\sigma(v)$) based on different pre-processing methods (TI and AMSI) are shown in figure 11. The equivalent size, w_e, is defined as:

$$w_e = \sqrt{w_s \times w_n} \tag{11}$$

where w_s and w_n are the window size in the tangential and normal directions for the adaptive stretched images in physical domain. Taking $U_{\text{gradient}} = 0.2 U_{\text{mainstream}}$ for example, the window size near the interface is 9×32 pixels and the equivalent interrogation window size is approximate to 16×16 pixels. Indeed, the random errors in the velocity distribution within the stretched area increase due to the particle image deformation. However, all the comparisons should be done in physical domain instead of the image space. As shown in figures 11(a) and (b), the bias errors $\beta(u)$ and $\beta(v)$ fluctuate with a fixed period that might be related to the pixel-locking phenomena.

As shown in figure 11(a), the variations of bias errors, $\beta(u)$, are negligible beyond the high-shear region. However, significant improvements in the accuracy for *u* component can be seen in the results for 'AMSI-0.2' and 'TI-32'. The differences between the adaptive meshing and stretching of the image method (AMSI) and the transformation method become smaller as the velocity gradient threshold increase. In addition, the adaptive meshing and stretching of image method (AMSI) is more accurate than a finer sampling rate based on conventional method and considerably faster. Figure 11(b) shows that the random errors, $\sigma(u)$, of adaptive meshing and stretching of the image method (AMSI) are smaller than 'TI-32', but higher than 'TI-16'. This can be explained by the reduction in the shear rate and decrease in the number of particles within a single interrogation window (particle density).

However, the bias and random errors of *v* component show different scenarios. As shown in figure 11(c), the differences of the bias errors distribution between different methods, except for 'TI-16', are modest beyond the region of high shear. The bias errors are of the same order of those near the wall for
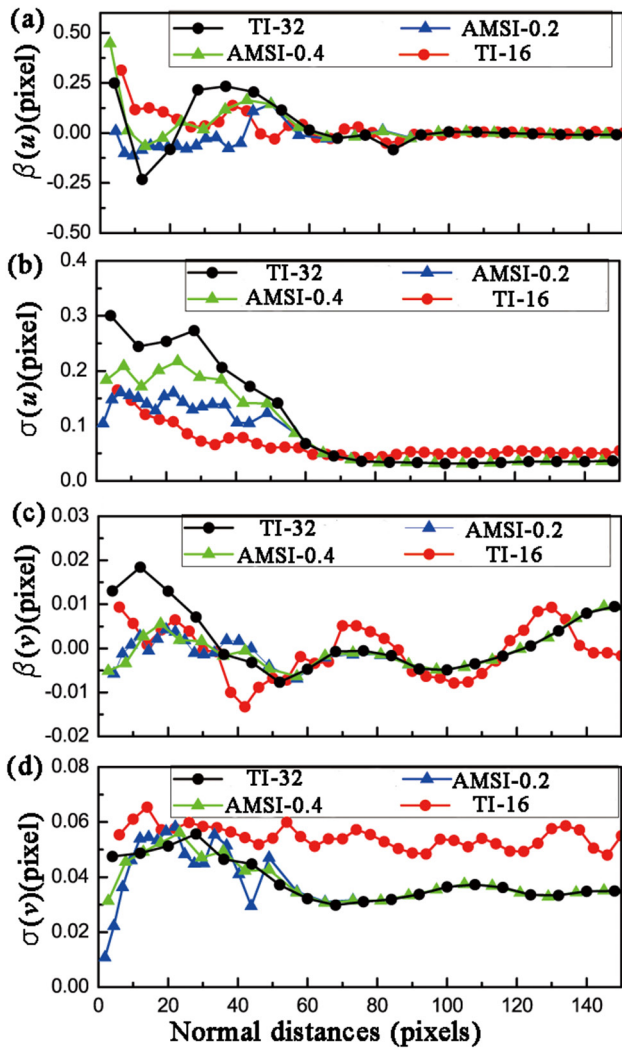
Figure 11. Bias errors and random errors distribution for different pre-processing methods: (a) bias errors distribution of tangential direction component, (b) random errors distribution of tangential direction component, (c) bias errors distribution of normal direction component, (d) random errors distribution of normal direction component.

distances beyond the high-shear region with the amplitude less than 0.01 pixel. Within the region of high shear, 'AMSI-0.2' and 'AMSI-0.4' are comparable, which are significantly better than 'TI-32' for most of this region, and significantly better than 'TI-16' near the wall and near the edge of the high-shear region. Compared with the distribution of $\beta(v)$, $\sigma(v)$ only fluctuates within a small range. 'AMSI-0.2' exhibits smaller random errors for the region below 10 pixels compared with the other methods. The higher bias errors and random errors in v component for 'TI-16' are mainly caused by the reduction of the number of particles within a single interrogation window. The differences for the two components are mainly due to the dominant role of the u velocity gradient. Similar trends in the bias and random error distribution were found for all the mainstream velocity cases.

The influence of the threshold gradients on random error distributions is shown in figure 12. The threshold gradients are normalized with the mainstream velocity, resulting in a
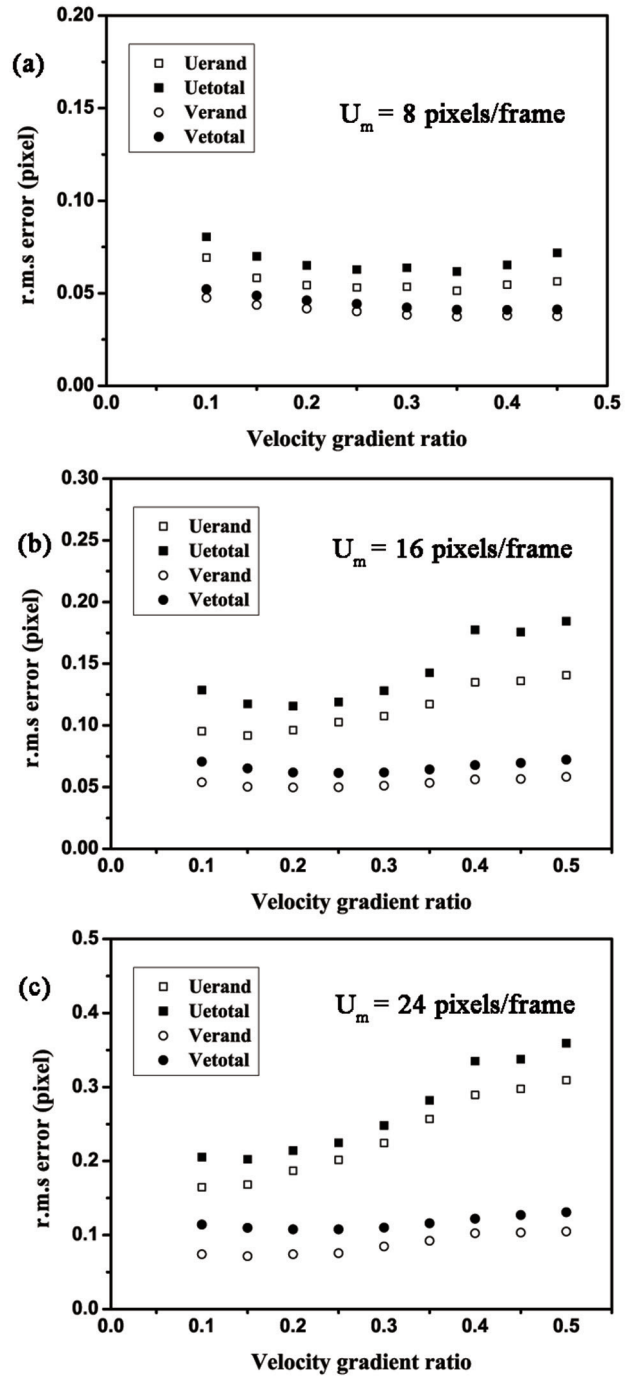

Figure 12. Random and total error distributions in the physical domain (x,y) for different image processing methods. (a) mainstream velocity $U_m = 8$ pixels/frame, (b) $U_m = 16$ pixels/frame, (c) $U_m = 24$ pixels/frame.

nondimensional velocity gradient ratio, λ, which ranges from 0 to 0.5. The effect of adaptive stretching in the near-wall image strips gradually weakens as the velocity gradient ratio increases. For the biggest λ, $\lambda = 0.5$, all the AMSI images and TI images are identical. The total error reaches a minimum near $\lambda = 0.25$ for the $U_m = 8$ pixels/frame case. Then, due to the reduction in the number of particles inside a single interrogation window, the total error increases when λ is less than 0.2. Nevertheless, the higher shear rate is responsible for
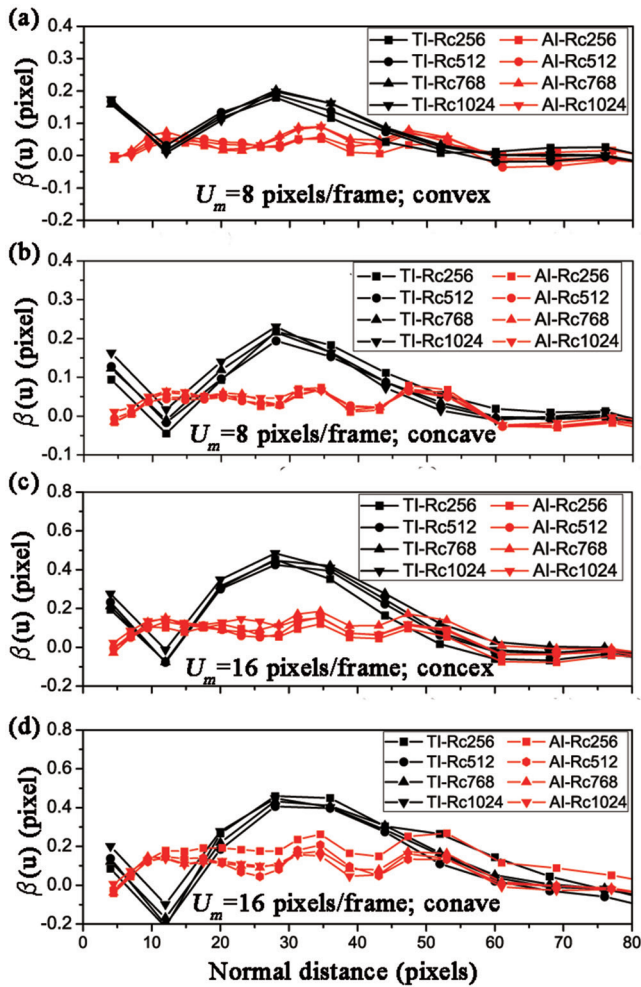
Figure 13. Bias error distributions in the tangential component for different radiuses of curvature for the different image processing methods.

the increased total and random errors for larger threshold gradients. The tendency varies as mainstream velocity increases, as shown in figures 12(b) and (c). For higher mainstream velocities, the optimum value of λ is roughly 0.2. The total and random errors increase as λ increases for both $U_m = 16$ and 24 pixels/frame cases, which means that the high-shear gradients dominate the error distributions for high-shear gradients.

The results in figure 13 show the influence of curvature on the bias error distribution for different mainstream velocities. The bias error distributions for TI method , as shown with black lines, are similar for both the convex and concave surfaces. The highest loss of accuracy occurs at the middle position and the near-wall region. The bias errors along the concave surface are higher than for the convex surface due to the distortion of velocity distribution and particle images. The bias error distributions for the AMSI method, as shown with red lines, are much smaller compared with the TI method within the high shear region for both the convex and concave surfaces. What's more, the variations of the bias errors only fluctuate within a range no more than 0.2 pixel for all the radiuses of curvature considered here. These results show the robustness of this adaptive meshing and stretching method.

The adaptive meshing and stretching of image method (AMSI) consumes more computational time in several aspects compared with the classical approach, as shown in figure 14(a). The pre-processing includes the background substraction and particle detection. Four multi-grid steps are applied, followed by two iterative loops, which is similar to the setup used by [24]. Figure 14(b) shows the relative computation times for the different sub-processes of AMSI method. The adaptive stretching of the images and the cross-correlation of the stretched images are in general the most computation demanding and will increase as the number of iterations increases. The computational time associated with these two steps is as much as 70%, which is higher than with adaptive PIV [24]. As mentioned in [24], the adaptive sampling and omission of superfluous correlation windows allowed the implemented technique to reduce the computation time by a factor of 2 compared to the classical approach. Thus, the AMSI method reduces the computation time by a factor of at least 2 compared to the classical approach, with improved spatial resolution and accuracy.

4. Experimental tests

This image pre-processing technique was used with real flows in three test experiments for a hypersonic turbulent boundary layer on a flat plate, a rotating blade and a flapping flag.

4.1. Supersonic turbulence boundary layer on a flat plate

The first experiment data set is used to verify the capability of this method to evaluate high-shear flows on a flat plate. The experiment was performed in a supersonic wind tunnel located at the National University of Defense Technology, Hunan. The facility has a rectangular cross-section of 100 mm × 120 mm. The light sheet for illuminating the particles was 0.5 mm thick. The camera resolution was 2048 pixels × 2048 pixels, corresponding to a 60 mm × 60 mm field of view. PIV images were obtained with a 492 m s^{-1} free stream velocity, which corresponds to Reynolds number Re $= 9 \times 10^6$ and Mach number Ma $= 3$. Nanometre titanium dioxide particles were used to sample the flow. The particle displacement in the freestream is nearly 90 pixels, which leads to a severe velocity gradient within the boundary layer. The interrogation window size (W_s) was set to 256×256 pixels at the beginning. In subsequent steps, the windows were gradually reduced to 64×64 pixels. The results of 255 pairs of recordings were averaged to give the average result. The average result was used to generate the adaptive stretched mesh. Figure 15 shows the PIV results with different processing methods normalized by the friction velocity, u_τ. The wall-shear stress was estimated from the logarithmic region of the boundary layer profile using Clauser method [2] as

$$\frac{u(y)}{u_\tau} = \frac{1}{K} \ln(\frac{y \cdot u_\tau}{\upsilon}) + B \qquad (12)$$

Here, $K = 0.41$ and $B = 5.1$. The evaluated profiles for different methods in the logarithmic region are nearly the same.
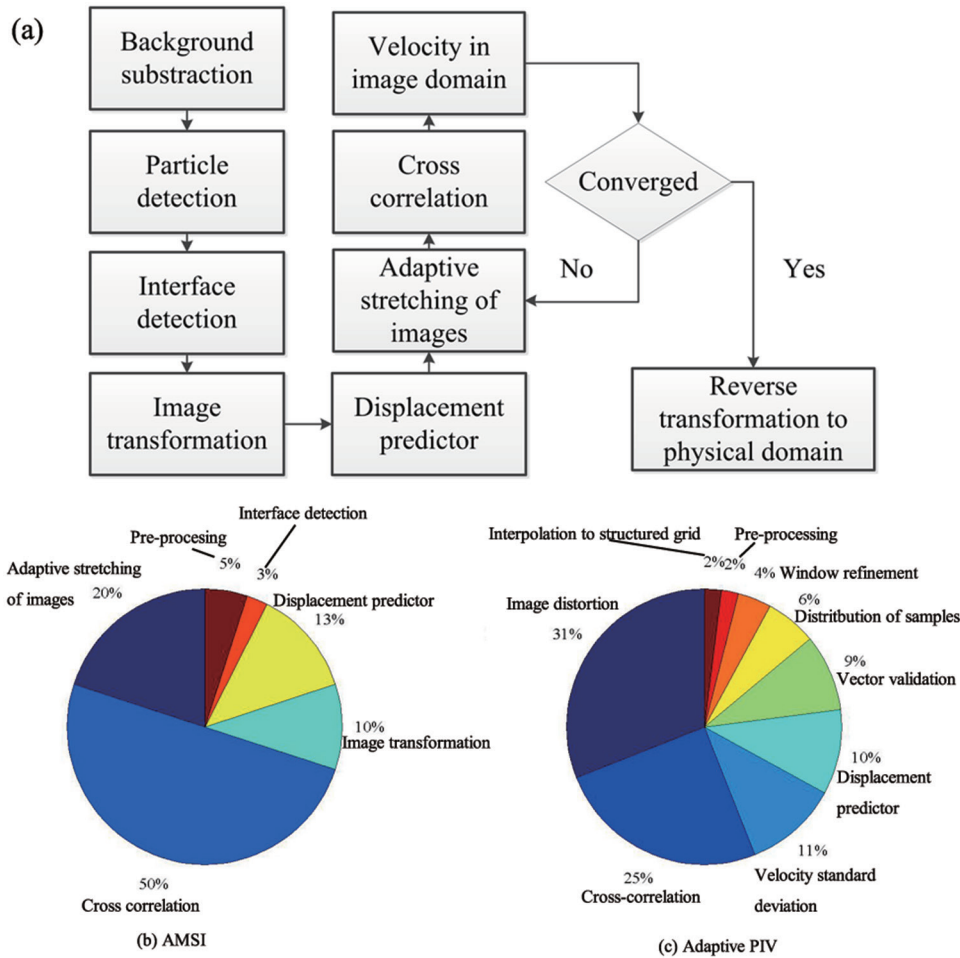
Figure 14. Block diagram of the implemented interrogation method (a) and distribution in relative computational time: (b) AMSI, (c) adaptive PIV.
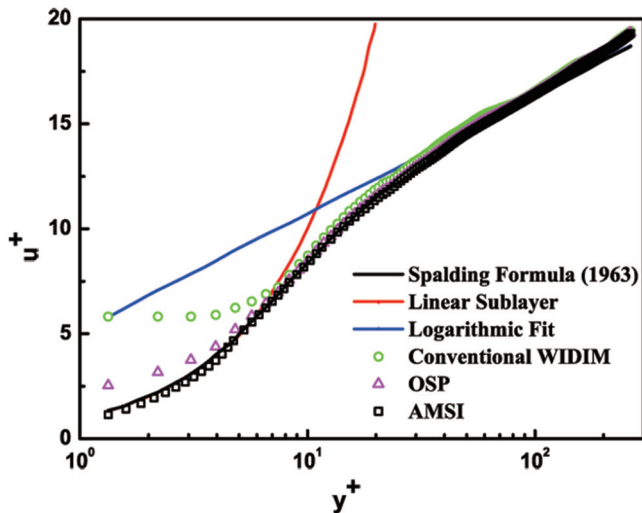

Figure 15. Comparison of the mean results of different PIV methods for a supersonic boundary layer on a flat plate.

u_τ was estimated as 9.76 m s^{-1}. Then, the Spalding formula was used as a indicator of physical tendency. As can be seen, the adaptive meshing and stretching of the image method (AMSI) gives higher spatial resolution and the best description of the profile in the viscous sub-layer.

4.2. Rotating blade surface

The second experiment was performed in a low speed wind tunnel with a turbulence level lower than 0.1%. The wind tunnel has a rectangular cross-section of 1.5 m × 1.5 m with the setup shown in figure 16. The blade rotational speed was varied from 600 rpm to 3000 rpm with a blade chord of 40 mm length. The hub radius was 60 mm with a hub-tip ratio of 0.6. The light sheet was at the 50% span position on the blade. A thicker airfoil profile, Göttingen387, was chosen for manufacturing considerations.

The laser sheet was illuminated for 4 ns with a highest pulse energy of 120 mJ Nd:YAG laser and a the wavelength of 532 nm. An $f = -50$ mm lens and a long focus $f = 1000$ mm lens were used to generate a light sheet 40 mm wide and 1 mm thick. The camera resolution was 1040 pixels × 1376 pixels, corresponding to a 20 mm × 25 mm field of view. The Reynolds number based on the chord and the mainstream velocity was 2.2×10^4. The sampling rate was 4 Hz and the time interval between successive images was d$t = 10$ μs. Smoke particles with a mean diameter of 1 μm were used as the tracer particles in the flow field. The window-correlation evaluations used 64 × 64 pixels for the coarse sample and 32 × 32 pixels as the final resolution sample with 75% overlap.
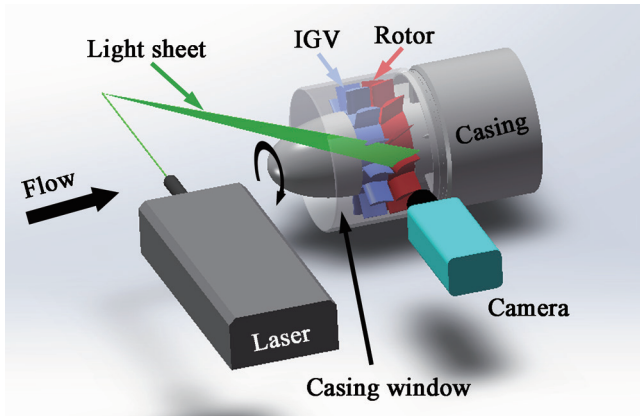
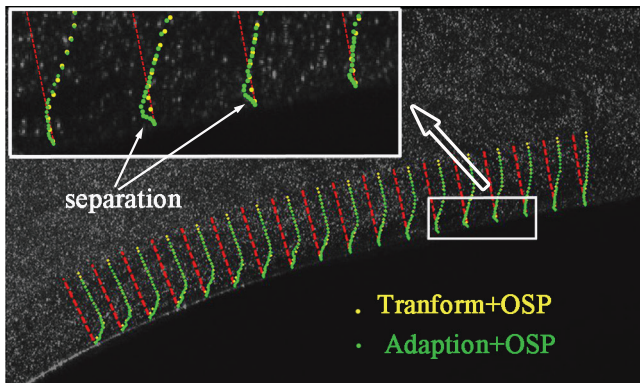**Figure 16.** Experimental configuration for the rotating blade.

Figure 17. Velocity distribution along the blade surface for the rotating blade.

The relative velocity profiles along the blade suction surface are shown in figure 17. The maximum displacement in the full image is about 12 pixels, and the boundary thickness is about 80 pixels. In fact, the real velocity distribution is not strictly known due to the difficulties in both experimental measurements and numerical simulations. However, the close-up of the white rectangular zone shows that the separation and reattachment can be captured by the AMSI method whose results are coincident with the flow visualization. The TI method did not capture these phenomena. The differences between TI and AMSI show that AMSI is able to evidence physical behavior that the other method misses, especially within the high shear region.

4.3. Flapping flag

Tests were also conducted with an elastic flag flapping experiment in a water tunnel with a rectangular test section of 0.4 m × 0.4 m × 3 m. The flag had heavy metal strips imbedded in a Polydimethylsiloxane sheet. The flexible yet self-supporting flag was placed in the water flow with the PIV system to measure the whole flow field around the mid-span of the flag. The leading edge of the elastic flag was fixed to a 1 mm diameter pole. The tests were performed with mainstream velocities ranging from 0.1 to 1.6 m s^{-1} with a turbulence level of approximately 0.1%. The Reynolds numbers based on the flag length and the mainstream velocity were in the range $\mathrm{Re}_L = 10^4$ 10^5.
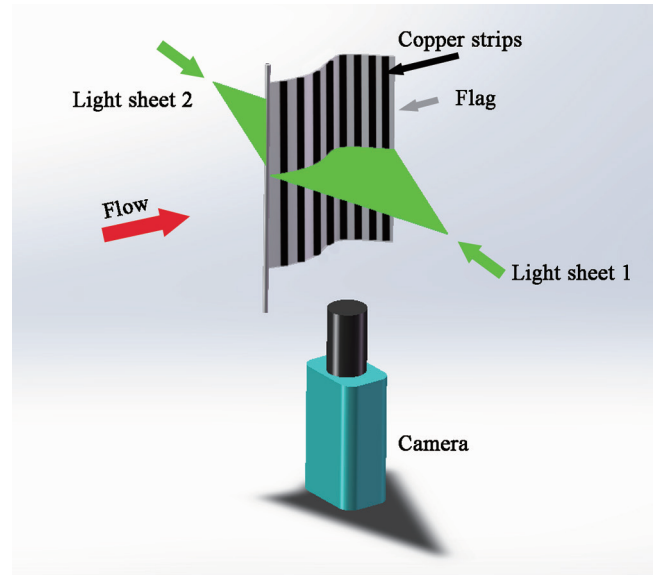

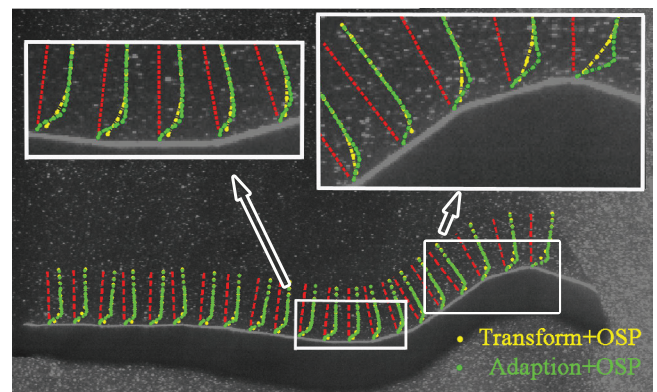**Figure 18.** Experimental configuration for the flapping flag.

Figure 19. Velocity distribution along the flag surface.

The PIV setup shown in figure 18 used a high speed CMOS camera with a 12 bit, 1024 pixels × 1024 pixels array and a 60 mm Nikon Micro lens to acquire the image sequences. The sampling rate was 2000 Hz and the time interval between adjacent images was 500 μs. The laser sheet passed through a glass window of the water tunnel, aligned with the flow and positioned at the mid-span of the elastic flag. Tracer particles with a mean diameter of 10 μm were injected into the test section to fill the water tunnel with a uniform density. The image pair post-processing used multiple passes with decreasing interrogation window sizes from 64 × 64 pixels down to 32 × 32 pixels and 75% overlap using the LaVison software with a Gaussian weighting function used in the cross-correlation calculations.

The relative velocity profiles along the flag surface are shown in figure 19. The maximum displacement in the full image was about 11 pixels. The boundary thickness is about 30 pixels, which is about the same size as interrogation window size. The close-up in two white rectangular zones showed no separation in either the AMSI or TI results. The velocity profiles show good agreement outside the boundary layer. Similar with the second test, the real velocity distribution is unknown either. However, the AMSI method gives a thinner boundary layer than the TI methods, which means a higher shear intensity

than the TI method. The difference between the AMSI and TI method is due to the average smoothing effect caused by the high shear within the interrogation windows near the interface.

5. Conclusions

This paper presents an approach for extracting accurate near-wall velocity profiles using an adaptive stretching image pre-processing method. This method includes an interface tracking technique using a Radon transform, a transformation to straighten the images at the curved interface and adaptive stretching of the image strips in the shear layer. The method gives higher spatial resolution in the wall-normal direction and low bias errors. The method was successfully benchmarked against the WIDIM technique using synthetic images and with three real images from a hypersonic turbulent boundary layer on a flat plate, laminar flow over a rotating blade and a flapping flag. The PIV measurements based on the AMSI images provide better agreement with the true values than the OI, SI and TI results and the smallest total errors ($\epsilon_{u,\text{total}}$ and $\epsilon_{v,\text{total}}$) of these four methods. The tests indicate that this adaptive meshing and stretching of the image method has higher spatial resolution for the velocity prediction in the shear layer with better performance. The optimum velocity gradient ratio, λ, roughly corresponds to 0.2 for mainstream velocities no bigger than 24 pixels/frame and shear layer thicknesses smaller than 80 pixels. The average smoothing effect caused by the large velocity difference and image distortion due to nonuniform stretching within the interrogation window can be effectively alleviated when the shear layer has been adaptively stretched, which presents robust velocity predictions for both the convex and concave surfaces. This method also has a relatively low computational cost compared with WIDIM (multiplied by the number of iterations) and the conventional adaptive meshing method.

Acknowledgments

References

[1] Adrian R J 1991 Particle-imaging techniques for experimental fluid mechanics *Ann. Rev. Mech.* **23** 261–304

[2] Clauser F H 1956 The turbulent boundary layer *Adv. Appl. Mech.* **4** 1–51

[3] Di Florio D, Felice F D and Romano G P 2002 Windowing, re-shaping and re-orientation interrogation windows in particle image velocimetry for the investigation of shear flows *Meas. Sci. Technol.* **13** 953–62

[4] Foroosh H, Zerubia J and Berthod M 2002 Extension of phase correlation to subpixel registration *IEEE Trans. Image Process.* **11** 188–200

[5] Gui L, Merzkirch W and Fei R 2000 A digital mask technique for reducing the bias error of the correlation-based PIV investigation algorithm *Exp. Fluids* **29** 30–5

[6] Gui L, Wereley S T and Kim Y H 2003 Advances and applications of the digital mask technique in particle image velocimetry experiments *Meas. Sci. Technol.* **14** 182028

[7] Hocharen M B and Fontaine A 2004 Wall shear-rate estimation within the 50cc Penn State artificial heart using particle image velocimetry *J. Biomech. Eng.* **126** 430–37

[8] Huang H T, Fiedler H E and Wang J J 1993 Limitation and improvement of PIV part II: particle image distortion, a novel technique *Exp. Fluids* **15** 263–73

[9] Jeon Y J and Sung H J 2011 PIV measurement of flow around an arbitrarily moving body *Exp. Fluids* **50** 787–98

[10] Lee C B and Wu J Z 2008 Transition in wall-bounded flows *Appl. Mech. Rev.* **61** 030802

[11] Liu B J, Yu X J, Liu H X, Jiang H K, Yuan H J and Xu Y T 2006 Application of SPIV in turbomachinery *Exp. Fluids* **40** 621–42

[12] Nguyen C V, Nguyen T D, Wells J C and Nakayama A 2010 Interfacial PIV to resolve flows in the vicinity of curved surfaces *Exp. Fluids* **48** 577–87

[13] Nguyen C V and Wells J C 2006 Development of PIV/interface gradiometry to handle low tracer density and curved walls *Proc. of FEDSM2006 European Fluids Engineering Summer Meeting (Miami, FL, USA, 17–20 July 2006)* (doi: 10.1115/FEDSM2006-98568)

[14] Nguyen C V, Wells J C 2006 Direct measurement of fluid velocity gradients at a wall by PIV image processing with stereo reconstruction *J. Vis.* **45** 5–27

[15] Nguyen T D, Wells J C and Nguyen C V 2012 Velocity measurements of near-wall flow over inclined and curved boundaries by extended interfacial particle image velocimetry *Flow Meas. Instrum.* **23** 33–9

[16] Park J, Im S, Sung H J and Park J S 2015 PIV measurements of flow around an arbitrarily moving free surface *Exp. Fluids* **56** 1–16

[17] Rohály J, Frigerio F and Hart D P 2002 Reverse hierarchical PIV processing *Meas. Sci. Technol.* **13** 984–96

[18] Ronneberger O, Raffel M and Kompenhans J 1998 Advanced evaluation algorithms for standard and dual plane particle image velocimetry *Proc. of the 9th Int. Symp. on Applications of Laser Techniques to Fluid Mechanics (Lisbon, 13–6 July 1998)*

[19] Scarano F 2002 Iterative image deformation methods in PIV *Meas. Sci. Technol.* **13** R1–19

[20] Scarano F 2003 Theory of non-isotropic spatial resolution in PIV *Exp. Fluids* **35** 268–77

[21] Scarano F and Riethmuller M L 1999 Iterative multigrid approach in PIV image processing with discrete window offset *Exp. Fluids* **26** 513–23

[22] Lee C B, Su Z, Zhong H J, Chen S Y, Zhou M D and Wu J Z 2013 Experimental investigation of freely falling thin disks. Part 2. Transition of three-dimensional motion from zigzag to spiral *J. Fluid Mech.* **732** 77–104

[23] Tang Q, Zhu Y D, Chen X and Lee C B 2015 Development of second-mode instability in a Mach 6 flat plate boundary layer with two-dimensional roughness *Phys. Fluids* **27** 064105

[24] Theunissen R, Scarano F and Riethmuller M L 2007 An adaptive sampling and windowing interrogation method in PIV *Meas. Sci. Technol.* **18** 275–87

[25] Theunissen R, Scarano F and Riethmuller M L 2008 On improvement of PIV image interrogation near stationary interfaces *Exp. Fluids* **45** 557–72

[26] Tisserant D and Breugelmans F A E 1997 Rotor blade-to-blade measurements using particle image velocimetry *J. Turbomach.* **119** 176–81

[27] Uzol O, Chow Y C, Katz J and Meneveau C 2002 Experimental investigation of unsteady flow field within a two-stage axial turbomachine using particle image velocimetry *J. Turbomach.* **124** 542–55

[28] Wernet M P 2000 Development of digital particle image velocimetry for use in turbomachinery *Exp. Fluids* **28** 97–115

[29] Zhong H J, Chen S Y and Lee C B 2011 Experimental study of freely falling thin disk: transition from planar zigzag to spiral *Phys. Fluids* **23** 011702

[30] Zhu Y D, Yuan H J, Zhang C H and Lee C B 2013 Image-preprocessing method for near-wall particle image velocimetry (PIV) image interrogation with very large in-plane displacement *Meas. Sci. Technol.* **24** 125302

[31] Zhu Y D, Yuan H J and Lee C B 2015 Experimental investigations of the initial growth of flow asymmetries over a slender body of revolution at high angles of attack *Phys. Fluids* **27** 084103

[32] Zhu Y D, Zhang C H, Chen X, Yuan H J, Wu J Z, Chen S Y and Lee C B 2016 Transition in hypersonic boundary layer: role of dilatational waves *AIAA J.* **54** 3039–49